The Astrophysical Journal, 890:56 (7pp), 2020 February 10 https://doi.org/10.3847/1538-4357/ab6a93

Synchrotron Gamma-Ray Emission Model of the Giant Outburst of Quasar 3C 279 in 2015 June: Fast Reconnection or Stochastic Acceleration with Electromagnetic Cascade?

Katsuaki Asano[1] and Masaaki Hayashida[2,3]
[1] Institute for Cosmic Ray Research, The University of Tokyo, 5-1-5 Kashiwanoha, Kashiwa, Chiba 277-8582, Japan; asanok@icrr.u-tokyo.ac.jp
[2] Department of Physics, Rikkyo University, 3-34-1 Nishi-Ikebukuro, Toshima-ku, Tokyo 171-8501, Japan; masaaki.hayashida@rikkyo.ac.jp
[3] Galaxies, Inc., 1-1-11 Minami-Ikebukuro, Toshima-ku, Tokyo, 171-0022, Japan
Received 2019 July 9; revised 2020 January 9; accepted 2020 January 10; published 2020 February 12

Abstract

We test the synchrotron emission scenario for the very bright gamma-ray flare of blazar 3C 279 observed in 2015 June using time-dependent numerical simulations. A bulk Lorentz factor as high as 100 can bring the synchrotron maximum energy above the GeV energy range. We find two possible solutions for the X-ray to gamma-ray spectrum. One is a prompt electron injection model with a hard power-law index as magnetic reconnection models suggest. Too strong a magnetic field yields too bright a synchrotron X-ray flux due to secondary electron–positron pairs. Even in the prompt electron injection model, the Poynting flux luminosity is at most comparable to the gamma-ray or electron luminosity. Another model is the stochastic acceleration model, which leads to a very unique picture accompanying the electromagnetic cascade and reacceleration of the secondary electron–positron pairs. In this model, the energy budget of the magnetic field is very low compared to gamma-rays and electrons.

Unified Astronomy Thesaurus concepts: Blazars (164)

1. Introduction

3C 279 is one of the most frequently studied flat spectrum radio quasars (FSRQs) at redshift $z = 0.536$. The *Fermi*-Large Area Telescope detected two prominent gamma-ray flares in 2013 December and 2015 June (Hayashida et al. 2015; Ackermann et al. 2016). The 2013 flare showed very hard spectrum with a photon index of 1.7 ± 0.1 above 100 MeV. Leptonic scenarios for that flare imply extremely low magnetization for the emission region (Asano & Hayashida 2015; Hayashida et al. 2015). In the 2015 flare, the gamma-ray flux is historically highest with the gamma-ray isotropic luminosity of $\sim 10^{49}$ erg s^{-1}. The two minute binned lightcurve shows a flux doubling timescale shorter than five minutes, which implies a very high bulk Lorentz factor such as $\Gamma > 50$.

The standard model for the gamma-ray emission in FSRQs is the inverse Compton scattering with external photons from the broad line region (BLR) or dust torus (EIC model, e.g., Sikora et al. 1994). Petropoulou et al. (2017) have discussed the 2015 June flare adopting a proton synchrotron model. Even with a super-Eddington jet luminosity and a smaller comoving source size than R/Γ, where R and Γ are the distance from the central black hole and the bulk Lorentz factor, respectively, the electromagnetic cascade initiated by photomeson production leads to a softer spectrum than the observed X-ray spectrum. Ackermann et al. (2016) have proposed an interesting alternative scenario: gamma-rays are originating as electron synchrotron emission from a highly magnetized plasma, contrary to the case in the 2013 flare.

In this paper, we investigate possibilities of such leptonic synchrotron models for the 2015 June gamma-ray flare with the time-dependent numerical code in Asano et al. (2014). If the gamma-ray flare is attributed to synchrotron emission, both the electrons emitting gamma-rays and X-rays promptly lose their energies. When electrons are injected with a power-law energy distribution of index $p > 2$ in the energy range responsible for the photon emission from X-ray to gamma-ray, in the fast cooling regime the photon index becomes $(p+2)/2 \geqslant 2$ (e.g., Dermer et al. 1997). Yet, the observed X-ray photon index is 1.17 ± 0.06 (Ackermann et al. 2016), significantly harder than 2. Even considering a minimum-energy of electrons at injection much higher than the bulk Lorentz factor as assumed in gamma-ray bursts (Sari et al. 1998), the cooled electrons below the minimum-energy result in a photon index 1.5. Such a high minimum-energy at injection can be regarded as the extremely hard limit for the low-energy portion of a broken power-law energy distribution.

In the synchrotron scenario, acceleration mechanisms that produce a hard spectrum of electrons are required. In this paper, we adopt a prompt power-law injection model ($p < 2$) and a stochastic acceleration model, which are motivated by magnetic reconnection and turbulence acceleration, respectively.

2. Model Setup

In this paper, we adopt the time-dependent numerical code in Asano et al. (2014; see also Asano & Hayashida 2015, 2018). In this code, the geometry of the jet is conical, and the evolution of the electron/photon energy distribution is calculated taking into account electron injection, photon production via synchrotron and inverse Compton, photon escape, radiative and adiabatic cooling of electrons, synchrotron self-absorption, $\gamma\gamma$ pair production, and attenuation by the extragalactic background light (EBL). Our code is based on the one-zone approximation so that the secondary pairs are injected into the same region and experience the same magnetic field. The 3C 279 photon spectrum shown in Ackermann et al. (2016) was obtained by averaging the flux over the orbital period of 95.6 minutes, which is much longer than the variability timescale. We took the photon spectra of the highest-flux orbit (Orbit C) and the subsequent orbit (Orbit D) for our studies of the emission modeling. The minute-scale variability in flux was observed in both the orbits, and the simultaneous *Swift* observational data for X-ray and UV ($W2$) bands are available during Orbit D. In this paper, we obtain

steady solutions of the emission, which can be regarded as the average emission over the orbital period. In this treatment, the temporal evolution of the electron/photon energy distribution in the jet frame is equivalent to the radial evolution in the steady jet (see Asano et al. 2014 for details).

The jet parameters are the initial radius R_0, the bulk Lorentz factor Γ, and the initial magnetic field B_0. The jet opening angle is assumed as $\theta_j = 1/\Gamma$. The emission released from various angles within θ_j is integrated with the exact beaming factor to obtain a spectrum for an on-axis observer. Though we cannot uniquely determine the parameter values, throughout this paper (except for model C0), we adopt $R_0 = 7.1 \times 10^{16}$ cm and $\Gamma = 100$, yielding a variability timescale $t_{\rm var} \simeq R_0/(c\Gamma^2) = 237$ s consistent with the observed one. Adjusting other parameters concerning electron injection/acceleration, we try to reproduce the gamma-ray flux by synchrotron emission. The adopted value of Γ is larger than the typical value for blazars ($\Gamma \sim 10$), but not unheard of. For example, the 2006 July flare of PKS 2155–304, which showed a gamma-ray (>200 GeV) variability on timescales of ~200 s, requires a large Lorentz factor $\gtrsim$100 to reconcile the variability with the broadband spectrum (Aharonian et al. 2007; Kusunose & Takahara 2008). As will be shown below, such a large Γ is required to explain the spectrum from X-ray to gamma-ray by synchrotron emission.

We divide the conical jet into shells with width of R_0/Γ^2 in the observer frame. The comoving volume of each shell for the one-side jet evolves as

$$V'_j = \frac{4\pi R_0^3}{\Gamma}\left(\frac{R}{R_0}\right)^2 \frac{(1-\cos\theta_j)}{2}, \quad (1)$$

with a distance R. Considering continuous ejection of identical shells from $R = R_0$, a steady outflow is realized in our computation. The magnetic field in the jet frame evolves as

$$B' = B_0\left(\frac{R}{R_0}\right)^{-1}. \quad (2)$$

The jet is surrounded by an external photon field coming from the BLR. The energy density and spectrum of the external photon filed in the jet frame are provided by the same model in Hayashida et al. (2012); the photon spectrum is the diluted Planck distribution with photon temperature of

$$T'_{\rm UV} = 10\Gamma \ {\rm eV}, \quad (3)$$

and the energy density is written as

$$U'_{\rm UV} = \frac{0.1\Gamma^2 L_D}{3\pi c R_{\rm BLR}^2 (1+(R/R_{\rm BLR})^3)}, \quad (4)$$

(Sikora et al. 2009),where L_D is the disk luminosity, and $R_{\rm BLR}$ is the size of the BLR,

$$R_{\rm BLR} = 0.1\left(\frac{L_D}{10^{46}\ {\rm erg\ s^{-1}}}\right)^{1/2} {\rm pc}. \quad (5)$$

For 3C 279, we adopt $L_D = 2 \times 10^{45}$ erg s^{-1} (Pian et al. 1999). The equipartition magnetic field with the photon energy density is $B_{\rm eq} = 91$ G at $R = R_0$. In Ackermann et al. (2016), the equipartition strength was estimated as 1.3 kG because of a lower bulk Lorentz factor ($\Gamma = 25$) they assumed ($B_{\rm eq} \propto \Gamma^{-3}$). Note that the high photon temperature in the comoving frame makes the Klein–Nishina effect significant for electrons with a Lorentz factor $\gamma'_{\rm e} > m_{\rm e}c^2/(4T'_{\rm UV}) \simeq 130$. Even for a lower magnetic field than $B_{\rm eq}$, the electron cooling is sensitive to the value of B'.

Table 1
Prompt Power-law Injection Model: Parameters

Model	Γ	R_0 (10^{16} cm)	B_0 (G)	p	$\gamma_{\rm max}$	$L_{\rm e,inj}$ (erg s^{-1})
A0	100	7.1	8.0	0.0	1.6×10^7	2.7×10^{45}
B0	100	7.1	80.0	0.2	5.0×10^6	2.7×10^{45}
C0	30	0.65	110.0	0.2	7.7×10^6	2.7×10^{45}

Note. The electron injection luminosity $L_{\rm e,inj}$ includes that for the counter jet.

3. Prompt Power-law Injection

First, motivated by the magnetic reconnection model, we test cases for electron injection with a power-law energy distribution with an exponential cut-off: $\dot{n}'(\gamma'_{\rm e}) \propto \gamma'^{-p}_{\rm e} \exp(-\gamma'_{\rm e}/\gamma_{\rm max})$. The strong magnetic field in our synchrotron model leads to prompt cooling of electrons. If the minimum electron energy at injection is low enough, the hard X-ray spectrum (see Figure 2) is inconsistent with the fiducial index $p \sim 2$ in the standard shock acceleration. However, the electron acceleration by magnetic reconnection can produce a very hard spectrum (e.g., Sironi & Spitkovsky 2014 and references therein). An electron injection with $p < 2$ is almost equivalent to a monoenergetic injection at the maximum energy. In this case, the prompt cooling yields a hard synchrotron spectrum with a photon index of 1.5.

Table 1 shows the model parameters. We inject electrons from the initial radius R_0 in the dynamical timescale R_0/c with luminosity of $L_{\rm e,inj}$ and very hard spectral index. Since almost all energy injected as electrons is converted to gamma-ray emission, the injection luminosity $L_{\rm e,inj}$ is the same for all models A0, B0, and C0. The minimum Lorentz factor $\gamma_{\rm min} = 100 \ll \gamma_{\rm max}$ is not an important parameter; the injected energy at $\gamma'_{\rm e} \sim \gamma_{\rm min}$ is negligible. Model B0 has a stronger magnetic field but lower maximum energy $\gamma_{\rm max}$ than those in model A0. To make a flat spectrum in the GeV energy range by the curved electron energy distribution around $\gamma_{\rm max}$, we need to keep the typical synhcrotron photon energy $\propto \Gamma B_0 \gamma^2_{\rm max}$ constant. In all the models, the combination $\Gamma B_0 \gamma^2_{\rm max}$ is adjusted to the same value, so that the gamma-ray spectra are almost identical in spite of different magnetic fields.

When we write the acceleration timescale as $t_{\rm acc} = \xi\gamma_{\rm e} m_{\rm e} c/(eB)$, where ξ is a dimensionless parameter, the balance with the cooling timescale, $t_{\rm c,syn} = 6\pi m_{\rm e} c/(\sigma_{\rm T} B^2 \gamma_{\rm e})$, provides us the maximum energy

$$\gamma_{\rm max} \simeq \sqrt{\frac{6\pi e}{\xi\sigma_{\rm T} B}} = 3.7 \times 10^7 \xi^{-1/2}\left(\frac{B}{10\ {\rm G}}\right)^{-1/2}. \quad (6)$$

Usually, ξ is assumed larger than unity, but the particle acceleration by magnetic reconnection would attain $\xi < 1$ (Cerutti et al. 2013). The values of $\gamma_{\rm max}$ in Table 1 imply that the acceleration efficiency is close to the limit of $\xi = 1$. The maximum synchrotron photon energy is independent of the

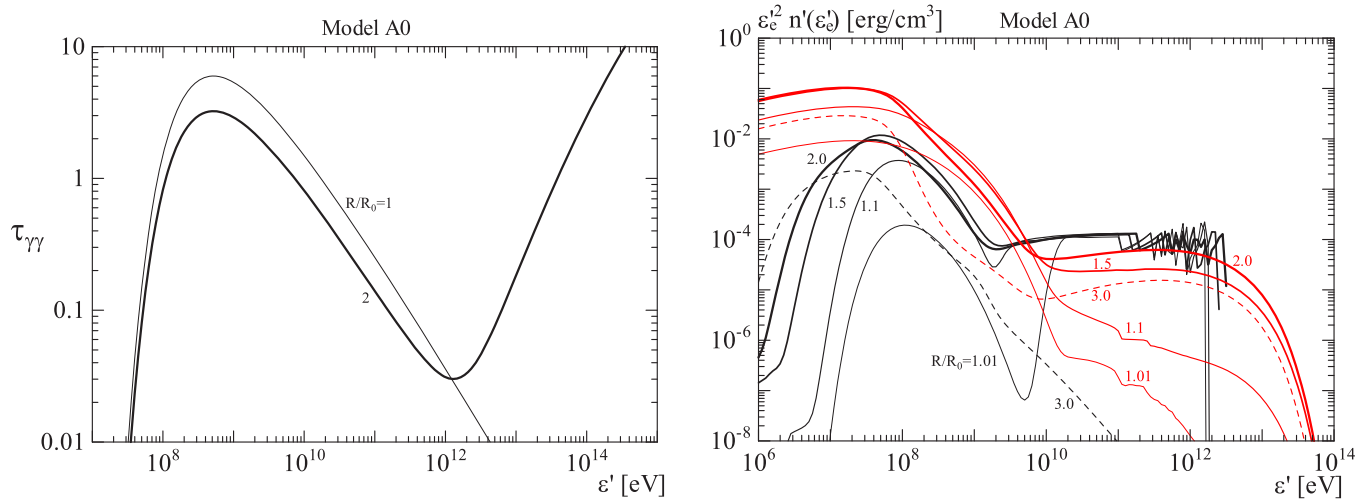

Figure 1. (Left) Optical depth for $\gamma\gamma$-absorption at $R = R_0$ (thin) and $2R_0$ (thick) in model A0. The photon energy is measured in the jet comoving frame. (Right) Evolution of the electron (black) and photon (red) energy distributions with increasing distance R (thin to thick) in model A0. The numbers beside each line denote R/R_0. Electrons are injected between $R = R_0$ and $2R_0$. At $R = 3R_0$ (thin dashed lines), the electron injection had been already stopped.

magnetic field as

$$\varepsilon_{\rm max} \simeq \Gamma \frac{3}{2}\frac{\hbar e B'}{m_{\rm e}c}\gamma'^{2}_{\rm max} = 24\xi^{-1}\left(\frac{\Gamma}{100}\right)\,{\rm GeV}. \quad (7)$$

The dominant target photons for $\gamma\gamma$-absorption is the external photon field. As the left panel in Figure 1 shows, the absorption effect becomes significant above $\varepsilon'_{\rm cut} \sim (m_{\rm e}c^2)^2/T'_{\rm UV} \sim 10^8\,{\rm eV}$ in the comoving frame. The cut-off energy for an observer is expected as $\Gamma\varepsilon'_{\rm cut} \sim 10\,{\rm GeV}$, which is almost independent of Γ.

In our code, while the calculation time step, which depends on electron energy, is always much shorter than the electron cooling timescale, the time steps for electron injection and calculation output are longer than the cooling timescale in the high energy range. Because of this time step effect, the electron energy distribution above $10^{11}\,{\rm eV}$ is noisy in the right panel in Figure 1. The electrons above $10^{12}\,{\rm eV}$ have been already cooled for this output time step. Since the emission is integrated with significantly short time steps, the photon spectrum is not affected by the output time step. As the electron spectra in Figure 1 shows, the cooled electrons distribute $n(\gamma'_{\rm e}) \propto \gamma'^{-2}_{\rm e}$ below $\gamma_{\rm max}$, which yields a photon spectrum $f(\varepsilon) \propto \varepsilon^{-0.5}$. However, the observed X-ray index is 0.2. To explain this harder X-ray spectrum, our numerical model needs additional parameters that describe a more complicated process/situation such as particle escape, and the decay or the inhomogeneity of magnetic field. We can see the spectral bump due to secondary electron–positron pairs around $10^8\,{\rm eV}$ in the electron spectra.

Model A0 in Figure 2 seems consistent with the gamma-ray spectrum and the UV flux. The flux level of the X-ray emission is also reproduced, though the spectrum is softer than the observed data as we have mentioned. The steep cut-off above 10 GeV is due to electron–positron pair absorption. The bump below 100 eV is the synchrotron emission by secondary electron–positron pairs. The increase of the optical depth above 1 TeV in Figure 1 at $R = 2R_0$ is due to the growth of the target photons for $\gamma\gamma$-absorption in the optical/IR band by this secondary synchrotron emission. In model B0, the higher secondary bump disagrees with the observed X-ray and UV flux. The magnetic luminosity, including the contribution of the

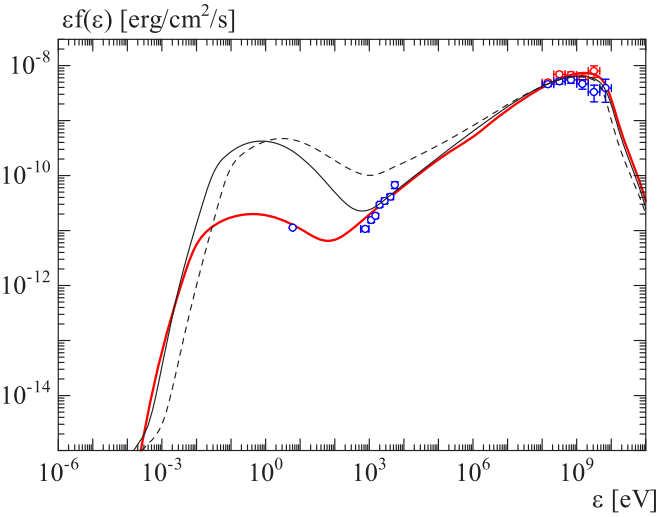

Figure 2. Photon spectra of the prompt power-law injection models. The model parameters are in Table 1. The red solid, thin black solid, and black thin dashed lines show the spectra for model A0, B0, and C0, respectively. The red and blue data points are observed data for Orbits C and D, respectively, in Ackermann et al. (2016) and Hayashida et al. (2017).

counter jet, is calculated as

$$L_B = 4\pi R_0^2\Gamma^2\left(\frac{B_0^2}{8\pi}\right)c(1-\cos\theta_j) \simeq \frac{1}{4}R_0^2 B_0^2\, c \quad (8)$$

$$\simeq 2.4\times 10^{45}\left(\frac{B_0}{8\,{\rm G}}\right)^2\left(\frac{R_0}{7.1\times 10^{16}\,{\rm cm}}\right)^2\,{\rm erg\,s^{-1}}, \quad (9)$$

which is comparable to the electron luminosity in model A0. Model B0 has difficulty also in the context of the energy budget, because the total magnetic luminosity of the source exceeds the Eddington luminosity; the Eddington luminosity is $8\times 10^{46}\,{\rm erg\,s^{-1}}$ for the black hole mass of $5\times 10^8\,M_\odot$. Therefore, the largely Poynting-flux-dominated jet, like model B0, is unlikely.

Since the observed variability provides an upper limit for R_0/Γ^2, a similar model to model A0 with a shorter R_0 keeping $B_0 = 8$ G and $L_{\rm e,inj}$ also yields the same successful spectrum.

Table 2
Stochastic Acceleration Model: Parameters and Energy Density Ratio

Model	B_0 (G)	K (s^{-1})	$\dot{N}_j$ (s^{-1})	U_B/U_e[a]
A	0.1	4.2×10^{-5}	2.5×10^{45}	2.7×10^{-4}
B	80	1.3×10^{-4}	6.7×10^{44}	180
C	0.1	4.2×10^{-4}	4.9×10^{32}	1.2×10^{-4}

Note. The other parameters $\Gamma = 100$ and $R_0 = 7.1 \times 10^{16}$ cm are common.
[a] The energy density ratio at $R = 2R_0$.

However, according to Equation (9), such a model leads to $L_{e,inj} \gg L_B$, which does not seem preferable for the magnetic reconnection model.

In model C0, we test a case with a lower Lorentz factor maintaining the variability timescale $R_0/(c\Gamma^2)$, typical synchrotron photon energy $\propto \Gamma B_0 \gamma_{max}^2$ and the luminosities $L_{e,inj}$ and L_B. The smaller R_0 required by the small Γ leads to a large magnetic field $B_0 \simeq 110$ G. Therefore, the secondary synchrotron emission becomes too luminous (see the thin dashed line in Figure 2). A high Lorentz factor is required for the prompt power-law injection model with the condition $L_B \gtrsim L_{e,inj}$.

4. Stochastic Acceleration Model

Here, let us consider the case in which electrons are gradually accelerated by turbulence as discussed in Asano et al. (2014), Asano & Hayashida (2015, 2018). The turbulence acceleration process, equivalent to the second order Fermi acceleration, can produce a harder spectrum than the standard shock acceleration. In this section, we show and compare results for both the EIC (models A and B) and the synchrotron (model C) emission scenario for gamma-rays. As will be shown below, the EIC models have difficulty in reconciling the gamma-ray with the X-ray and optical data.

The turbulence acceleration is expressed by the energy diffusion coefficient,

$$D'_{\gamma\gamma} = K\gamma_e'^2, \tag{10}$$

where the parameter K is constant. In this paper, we assume the hard-sphere type acceleration ($D'_{\gamma\gamma} \propto \gamma_e'^2$). As Asano & Hayashida (2015, 2018) show, the hard-sphere acceleration can reproduce broadband spectra for several blazars. The acceleration timescale ($\sim K^{-1}$) in this model is constant irrespective of particle energy. While the acceleration timescale for the highest-energy particles can be comparable to that frequently assumed in the shock acceleration models, lower-energy particles are accelerated with much longer timescales than their gyromotion period. The hard-sphere type acceleration can be caused by large-scale hydrodynamical eddy-turbulence (e.g., Ptuskin 1988; Cho & Lazarian 2006) or compressional magnetohydrodynamic waves (Teraki & Asano 2019). When the magnetic field energy is dominant (model B), the turbulence acceleration would show a different behavior from that in a weakly magnetized plasma (Demidem et al. 2019). However, for simplicity, we use Equation (10) throughout this section.

We inject electrons at a constant rate $\dot{N}_j$ into the volume V'_j from $R = R_0$ to $2R_0$. The initial Lorentz factor of electrons is $\gamma'_{inj} = 10$. For $R > 2R_0$, the injection and energy diffusion are halted.

The model parameters are summarized in Table 2. The shape of the spectrum is determined by the combination of B_0 and K. The injection rate $\dot{N}_j$ is adjusted to match the gamma-ray flux level. The UV flux may have a different origin from that for the gamma-ray flare, as discussed in Asano & Hayashida (2015). The UV data point can be regarded as the upper limit for the synchrotron component. First, in model A, we test the usual external inverse Compton (EIC) model. The flat gamma-ray spectrum is reproduced by Compton-scattered UV photons as shown in Figure 3. However, the narrow EIC spectral hump does not agree with the observed X-ray flux. Another component such as emission from a different region is needed for X-ray emission in this case. In our model, as electrons are injected and accelerated as far as $R = 2R_0$, the electron energy density becomes maximum at $R = 2R_0$. The energy density ratio of the magnetic field to the electron energy density U_B/U_e at $R = 2R_0$ is listed in Table 2. In model A, the magnetic field is much weaker than the equipartition value.

In model B, we adopt a stronger magnetic field. As shown in Figure 4, in spite of the larger diffusion coefficient, the cooling effect by the strong magnetic field suppresses the maximum energy of electrons compared to model A. Model B roughly reproduces the X-ray spectrum by synchrotron self-Compton emission in addition to the EIC gamma-ray spectrum. However, the synchrotron flux in the optical-UV band is extremely brighter than the UV data point and historical data by three orders of magnitude. Furthermore, as mentioned for model B0 in the previous section, $B_0 = 80$ G seems too large compared to the Eddington luminosity.

As the gamma-ray photon density is constrained by the observed flux, the numbers of the secondary pairs in both models A and B would be the same order as those in models A0 or B0. The low magnetic field in model A and the high synchrotron flux by the primary electrons in model B inhibit emergence of a distinct spectral component due to secondary pairs.

In our stochastic acceleration model, to increase the maximum electron energy, a lower magnetic field is preferable. In model C, we decrease the magnetic field again, and increase the diffusion coefficient. The cascade process with reacceleration, which will be discussed later, produces a flat electron/positron energy distribution, as shown in Figure 5. As we have mentioned in Section 2, electrons of $\gamma'_e > 130$ ($\varepsilon'_e = \gamma'_e m_e c^2 \sim 70$ MeV) are in the Klein–Nishina regime for the target photons of $4T'_{UV} = 4$ keV. The typical photon energy of IC emission in this regime is $\sim \Gamma \gamma'_e m_e c^2$. The electron energy distribution and the EIC photon spectrum of the previous EIC model, A (Figure 3), show that electrons around $\varepsilon'_e = 70$ MeV emit GeV gamma-rays via EIC. In model C, electrons/positrons with much higher energies than $\varepsilon'_e = 70$ MeV energetically dominate. Although such high-energy particles can emit gamma-rays via EIC emission in spite of the Klein–Nishina effect, the EIC photon energy ($\varepsilon \gg 70\Gamma$ MeV $= 7$ GeV) is much higher than the energy range of *Fermi*. The IC photons emitted by electrons with $\varepsilon'_e \gg 70$ MeV are promptly absorbed, and produce secondary electron–positron pairs. As a result, the IC photons emitted by the high-energy particles almost do not contribute to the flux below 7 GeV. Only gamma-rays in a narrow energy range between $\varepsilon'_{cut} \sim 100$ MeV and 2×70 MeV produce secondary pairs that emit gamma-rays below 7 GeV via EIC.

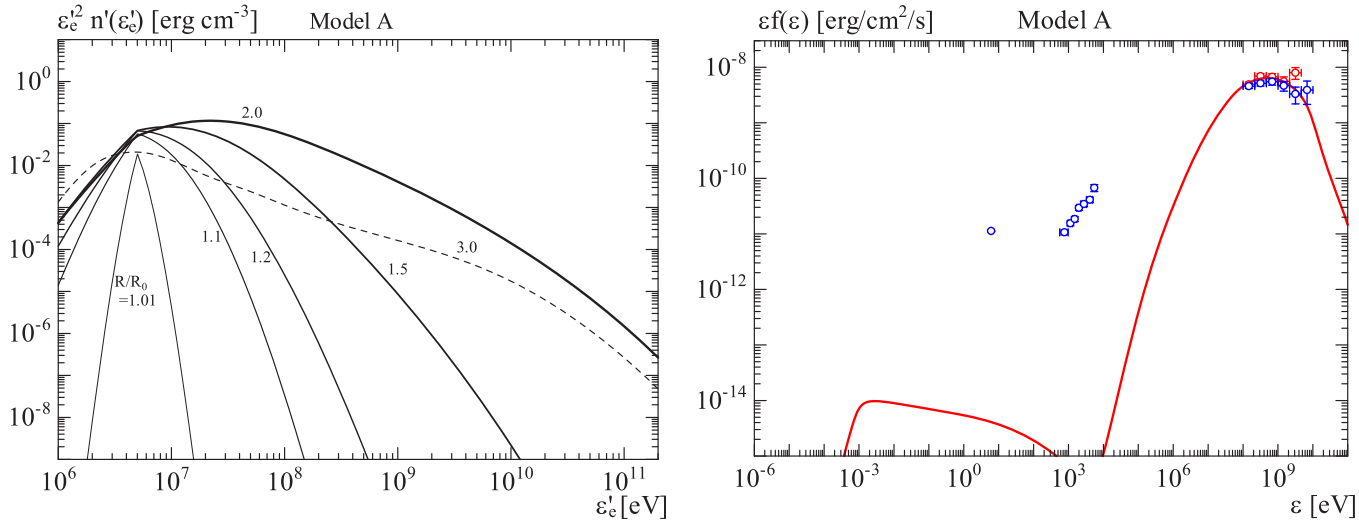

Figure 3. (Left) Evolution of the electron energy distribution (including secondary electron–positron pairs) with increasing distance R (thin to thick) in model A. The numbers beside each line denote R/R_0. Electrons are injected and accelerated between $R = R_0$ and $2R_0$. At $R = 3R_0$ (thin dashed line), the electron injection and acceleration had been already stopped. (Right) Photon spectrum for model A (red). The observed data are the same as in Figure 2.

Even though the magnetic energy density in model C is much lower than the photon energy density, high-energy electrons/positrons emit synchrotron photons, and cool mainly via synchrotron because of the Klein–Nishina effect. The maximum electron energy reaches $\sim 10^{14}$ eV as shown in Figure 5, which is consistent with the energy where cooling and acceleration balances as $t'_{\rm c,syn} = 1/K$. The typical energy of synchrotron emission is in the gamma-ray range as

$$\varepsilon_{\rm syn,typ} = \Gamma \frac{3\hbar e B_0}{2 m_{\rm e} c} \gamma_{\rm e}'^2 \tag{11}$$

$$\simeq 7 \left(\frac{\Gamma}{100}\right)\left(\frac{B_0}{0.1\ {\rm G}}\right)\left(\frac{\varepsilon'_{\rm e}}{10^{14}\ {\rm eV}}\right)^2 {\rm GeV}. \tag{12}$$

The gamma-ray photons *Fermi* detected are mainly emitted via synchrotron emission in this model, while EIC emission by low-energy particles slightly contribute to the gamma-ray flux. The factor ξ for those highest energy particles is ~ 3 (see Equations (6) and (7)).

Below we discuss the details of the very complicated cascade process with secondary pair injection, reacceleration, and the Klein–Nishina effect. In model C, secondary electron–positron pairs produced via $\gamma\gamma$-absorption are also accelerated by turbulence. Even with a very low injection rate (Table 2), the secondary pair production and the reacceleration attain the electron energy density/distribution required to reproduce the observed photon flux. The short acceleration timescale boosts the maximum electron energy, which leads to a high gamma-ray production rate at $\varepsilon' > \varepsilon'_{\rm cut} \sim 100$ MeV, where $\gamma\gamma$-absorption is efficient. The number of electrons/positrons is largely dominated by secondary pairs. The synchrotron peak energy in the jet comoving frame ($\sim$70 MeV) is almost the same as the $\gamma\gamma$-cut-off energy (see the left panel in Figure 1). Secondary electron–positron pairs are injected above $\varepsilon'_{\rm e} \sim 70/2$ MeV $= 35$ MeV.

The cooling time of electrons in the Klein–Nishina regime is almost the same as the scattering timescale, $t'_{\rm sc} = 1/(n'_{\rm UV}\sigma_{\rm KN} c)$. Adopting the photon density $n'_{\rm UV} \sim U'_{\rm UV}/(4T'_{\rm UV})$ and the cross section $\sigma_{\rm KN} \sim (3/8)\sigma_{\rm T} x^{-1}(\ln 2x + 1/2)$, where $x = 4T'_{\rm UV}\gamma'_{\rm e}/(m_{\rm e}c^2) \simeq \gamma'_{\rm e}/130$, we find that the synchrotron cooling becomes the dominant cooling process for particles above $\varepsilon'_{\rm e} \sim 90$ GeV.

Around 70 MeV, the IC cooling timescale ($\sim 10^3$ s) of electrons/positrons is comparable to the acceleration timescale $K^{-1} \sim 2000$ s, and the secondary injection is the most efficient in this energy range. Above this energy, the IC cooling timescale grows with energy owing to the Klein–Nishina effect. Namely, the IC cooling timescale for electrons between $\varepsilon'_{\rm e} = 70$ MeV and 90 GeV is longer than the acceleration timescale, but still shorter than the synchrotron cooling timescale $t'_{\rm c,syn} \propto \varepsilon'^{-1}_{\rm e}$. In this electron energy range, the radiative cooling, dominated by IC emission, is the subdominant effect compared to the stochastic acceleration, and the energy of IC photons emitted by such electrons is much higher than the *Fermi* energy range. For particles above $\varepsilon'_{\rm e} \sim 90$ GeV, the energy loss rate due to synchrotron emission becomes larger than the IC energy loss rate, and the total cooling timescale starts to decrease with energy. The cooling timescale becomes comparable to the acceleration timescale again at $\varepsilon'_{\rm e} \simeq 10^{14}$ eV.

If we neglect the reacceleration and the Klein–Nishina effect (the cooling timescale $\propto \gamma_{\rm e}^{-1}$), the particle energy distribution becomes as soft as $n'(\varepsilon'_{\rm e}) \propto \varepsilon'^{-(p+1)}_{\rm e}$, where $p \sim 2$ is the power-law index at the secondary injection. The Klein–Nishina effect would make the spectrum harder than the above estimate. On the other hand, if we only consider the acceleration and injection at $\gamma'_{\rm inj} = 10$, the spectrum is proportional to $\varepsilon'^{-1}_{\rm e}$ in the steady hard-sphere model. Our numerical result shows that the complex combination of the above effects leads to a spectrum slightly harder than $\varepsilon'^{-2}_{\rm e}$.

The synchrotron cooling time of the X-ray emitting electrons/positrons ($\varepsilon'_{\rm e} \simeq 3.9 \times 10^{10}(\varepsilon/1\ {\rm keV})^{1/2}$ eV) is $t'_{\rm c,syn} \simeq 10^6(\varepsilon/1\ {\rm keV})^{-1/2}$ s, which is much longer than the dynamical timescale $t'_{\rm var} = R_0/(c\Gamma) \simeq 2.4 \times 10^4$ s. In this case, the dominant cooling process is the adiabatic cooling, whose timescale is equal to the dynamical timescale. Even in the X-ray band, the variability timescale is regulated by the dynamical one $t_{\rm var} \simeq R_0/(c\Gamma^2)$ for an observer (see Asano et al. 2014). The synchrotron photon energy emitted by the electrons whose cooling timescale satisfy $t'_{\rm c,syn} = t'_{\rm var}$ is

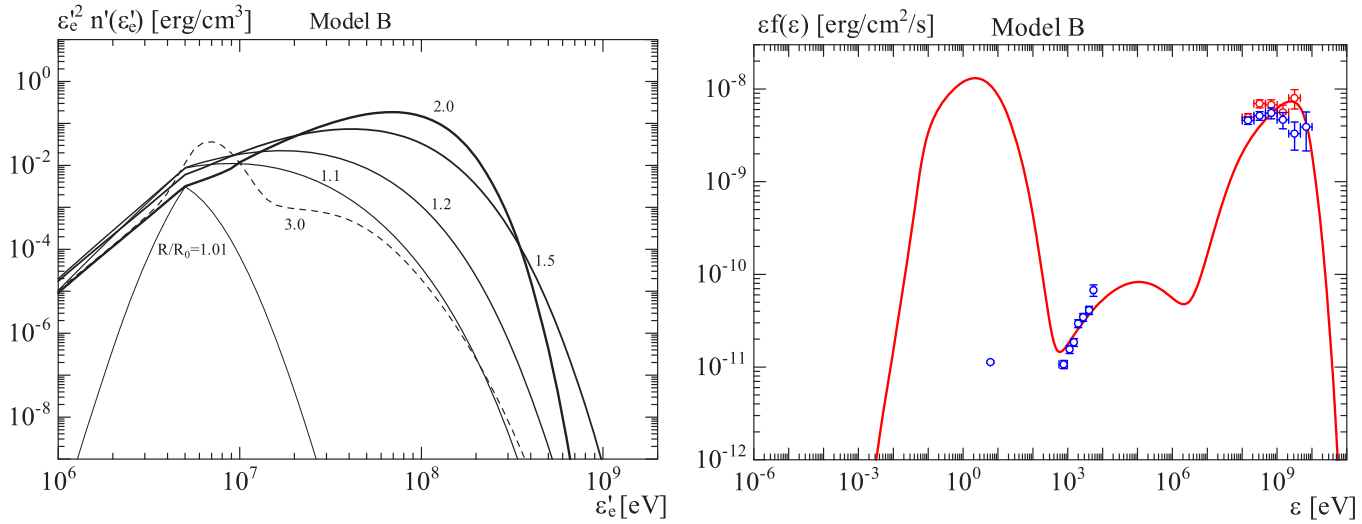

Figure 4. (Left) Evolution of the electron energy distribution (including secondary electron–positron pairs) with increasing distance R (thin to thick) in model B. The numbers beside each line denote R/R_0. Electrons are injected and accelerated between $R = R_0$ and $2R_0$. At $R = 3R_0$ (thin dashed line), the electron injection and acceleration had been already stopped. (Right) Photon spectrum for model B (red). The observed data are the same as in Figure 2.

$\sim$2 MeV, which corresponds to the cooling break in the photon spectrum in Figure 5.

The synchrotron spectrum in model C reproduces both the gamma-ray and X-ray data very well. The gamma-ray spectrum is mainly produced by synchrotron emission from the secondary pairs with a partial contribution of EIC emission. If we neglect the secondary pairs, the gamma-ray spectrum becomes dim and hard as shown by the blue line in the right panel of Figure 5. This synchrotron model with electromagnetic cascade is a very unique model to account for bright gamma-ray emission. To emit gamma-rays via synchrotron by electrons, a strong magnetic field is not necessarily required.

Recently, Abdalla et al. (2019) reported the sub-TeV gamma-ray detection by H.E.S.S. from the same 2015 June flare, though the observation time was not simultaneous with Orbits C and D (about 13 hr later). In our model C, the highest energy of electrons is 100 TeV, and most of the very-high-energy gamma-ray photons with energies $\varepsilon \gg 7$ GeV generated via EIC emission are absorbed in the source. A small fraction of such photons escape from the source as seen in Figure 5. The sharp cut-off above 100 GeV is due to EBL absorption. The sub-TeV photon flux in our model seems consistent with the observed flux, a few times 10^{-11} erg cm^{-2} s^{-1}.

5. Summary and Discussion

The very bright gamma-ray flare of 3C 279 in 2015 June can be explained by synchrotron emission. The assumed parameters $R_0 = 7.1 \times 10^{16}$ cm and $\Gamma = 100$ are consistent with the variability timescale. Motivated by the magnetic reconnection model, we have tested prompt electron injection with a power-law energy distribution with exponential cut-off. The required maximum energy of electrons is close to the limit of $\xi = 1$. If we adopt a strong magnetic field, the synchrotron emission from secondary electron–positron pairs is unavoidable. In order to reconcile the X-ray and UV fluxes, the magnetic field is at most 8 G. The production efficiency of secondary particles depends on the detail of the high-energy cut-off shape of the injected electron spectrum (Aharonian et al. 1986; Zirakashvili & Aharonian 2007). However, to reduce the secondary synchrotron flux by adjusting the cut-off shape, a fine tuned parameter set is required. A largely Poynting-flux-dominated jet is unlikely in terms of the X-ray spectrum and the energy budget.

We have also considered the stochastic acceleration model, in which the particle acceleration is phenomenologically expressed by the diffusion coefficient $D_{\gamma\gamma}$. Thanks to our time-dependent code, we have obtained a very unique picture accompanying the electromagnetic cascade and reacceleration of the secondary electron–positron pairs. The magnetization in this model is very low as $U_B/U_e \sim 10^{-4}$. Therefore, the synchrotron model for this flare does not necessarily mean a higher magnetization than the typical values in other blazars.

In our stochastic acceleration model with the electromagnetic cascade, the acceleration timescale, $K^{-1} \sim 2000$ s, does not depend on the electron energy. This type of acceleration can be realized by wave-particle interaction via transit-time damping. Considering the negligible energy fraction of the magnetic energy, let us focus on the fast MHD waves, in which the wave energy is dominated by kinetic energy rather than magnetic energy. If the turbulence injected at the scale of R_0/Γ with the relativistic sound velocity $c/\sqrt{3}$ cascades to shorter scales with a shortest scale $\lambda_{\rm min}$, according to the simulation in Teraki & Asano (2019), the diffusion coefficient is

$$K \simeq 5.6\frac{\pi}{18}c\left(\frac{R_0}{\Gamma}\right)^{-1/3}\lambda_{\rm min}^{-2/3}, \quad (13)$$

where the Kolmogorov turbulence is assumed. Our model C requires $\lambda_{\rm min} = 2.2 \times 10^{13}$ cm, which is 3% of the injected scale R_0/Γ. The shortest wave length $\lambda_{\rm min}$ should be longer than the Larmor radius of electrons to realize the hard-sphere acceleration. From $B_0 = 0.1$ G and the highest electron energy 10^{14} eV, we obtain a Larmor radius 3.3×10^{12} cm, which is consistently shorter than $\lambda_{\rm min}$. As a matter of course, the implied value of the acceleration timescale parameter is $\xi \sim 3$ at 10^{14} eV as we have mentioned in the previous section. Hydrodynamical eddy turbulences with a similar scale also induce the hard-sphere acceleration. Although we have an unknown parameter $\lambda_{\rm min}$,

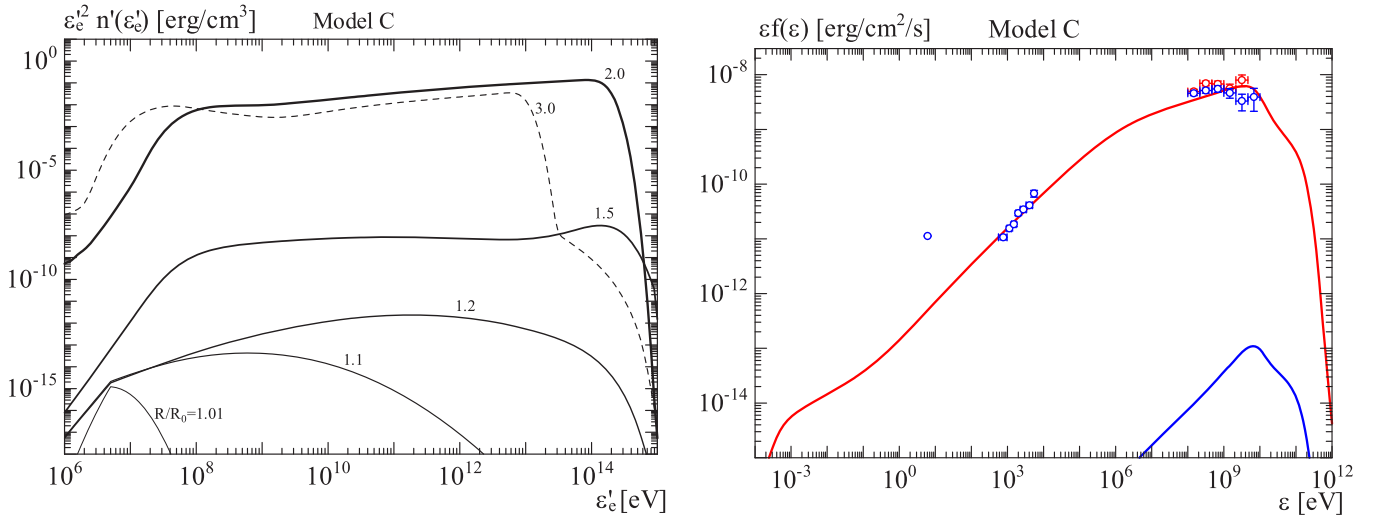

Figure 5. (Left) Evolution of the electron energy distribution (including secondary electron–positron pairs) with increasing distance R (thin to thick) in model C. The numbers beside each line denote R/R_0. Electrons are injected and accelerated between $R = R_0$ and $2R_0$. At $R = 3R_0$ (thin dashed line), the electron injection and acceleration had been already stopped. (Right) Photon spectrum for model C (red). The blue line shows the case neglecting the secondary electron–positron pairs. The observed data are the same as in Figure 2.

which may depend on the detail of the time-dependent energy transfer process between waves and particles with back-reaction, the required acceleration efficiency seems consistent with the turbulence acceleration picture.

The authors thank the anonymous referees for the valuable and helpful comments. This work is supported by the joint research program of the Institute for Cosmic Ray Research (ICRR), the University of Tokyo.

ORCID iDs

Katsuaki Asano https://orcid.org/0000-0001-9064-160X
Masaaki Hayashida https://orcid.org/0000-0003-2252-3411

References

Abdalla, H., Adam, R., Aharonian, F., et al. 2019, A&A, 627, A159
Ackermann, M., Anantua, R., Asano, K., et al. 2016, ApJL, 824, L20
Aharonian, F., Akhperjanian, A. G., Bazer-Bachi, A. R., et al. 2007, ApJL, 664, L71
Aharonian, F. A., Atoyan, A. M., & Nahapetian, A. 1986, A&A, 162, L1
Asano, K., & Hayashida, M. 2015, ApJL, 808, L18
Asano, K., & Hayashida, M. 2018, ApJ, 861, 31
Asano, K., Takahara, F., Kusunose, M., Toma, K., & Kakuwa, J. 2014, ApJ, 780, 64
Cerutti, B., Werner, G. R., Uzdensky, D. A., & Begelman, M. C. 2013, ApJ, 770, 147
Cho, J., & Lazarian, A. 2006, ApJ, 638, 811
Demidem, C., Lemoine, M., & Casse, F. 2019, arXiv:1909.12885
Dermer, C. D., Sturner, S. J., & Schlickeiser, R. 1997, ApJS, 109, 103
Hayashida, M., Madejski, G. M., Blandford, R., et al. 2017, in AIP Conf. Proc. 1792, 6th International Meeting on High Energy Gamma-Ray Astronomy, ed. F. A. Aharonian, W. Hofmann, & F. M. Riegerin (Melville, NY: AIP), 050015
Hayashida, M., Madejski, G. M., Nalewajko, K., et al. 2012, ApJ, 754, 114
Hayashida, M., Nalewajko, K., Madejski, G. M., et al. 2015, ApJ, 807, 79
Kusunose, M., & Takahara, F. 2008, ApJ, 682, 784
Petropoulou, M., Nalewajko, K., Hayashida, M., & Mastichiadis, A. 2017, MNRAS, 467, L16
Pian, E., Urry, C. M., Maraschi, L., et al. 1999, ApJ, 521, 112
Ptuskin, V. S. 1988, SvAL, 14, 255
Sari, R., Piran, T., & Narayan, R. 1998, ApJL, 497, L17
Sikora, M., Begelman, M. C., & Rees, M. J. 1994, ApJ, 421, 153
Sikora, M., Stawarz, Ł., Moderski, R., Nalewajko, K., & Madejski, G. M. 2009, ApJ, 704, 38
Sironi, L., & Spitkovsky, A. 2014, ApJL, 783, L21
Teraki, Y., & Asano, K. 2019, ApJ, 877, 71
Zirakashvili, V. N., & Aharonian, A. 2007, A&A, 465, 695